



# Modeling study of the impact of complex terrain on the surface energy and hydrology over the Tibetan Plateau

Xuehua Fan<sup>1</sup> · Yu Gu<sup>2</sup> · Kuo-Nan Liou<sup>2</sup> · Wei-Liang Lee<sup>3</sup> · Bin Zhao<sup>2</sup> · Hongbin Chen<sup>1</sup> · Daren Lu<sup>1</sup>

Received: 26 November 2018 / Accepted: 28 August 2019  
© Springer-Verlag GmbH Germany, part of Springer Nature 2019

## Abstract

The long-term effects of complex terrain on solar energy distributions and surface hydrology over the Tibetan Plateau (TP) are investigated using the 4th version of the global Community Climate System Model (CCSM4) coupled with a 3-D radiative transfer (RT) parameterization. We examine the differences between the results from CCSM4 with the 3-D RT parameterization and the results from CCSM4 with the plane-parallel RT scheme. In January (winter), the net surface solar flux (FSNS) displays negative deviations over valleys and the north slopes of mountains, especially in the northern margin of the TP, as a result of the 3-D shadow effect. Positive deviations in FSNS in January are found over the south slopes of mountains and over mountain tops, where more solar flux is intercepted. The deviations in total cloud fraction and snow water equivalent (SWE) exhibit patterns opposite to that of FSNS. The SWE decreases due to the 3-D mountain effect in spring and the magnitude of this effect depends on the terrain elevations. The SWE is reduced by 1–17 mm over the TP in April, with the largest decrease in SWE at an elevation of 3.5–4.5 km. Negative deviations in precipitation are found throughout the year, except in May and December, and they follow the seasonal variations in the deviations in total cloud fraction. The total liquid runoff at 3.5–4.5 km elevation increases in April due to earlier (March) snowmelt caused by increased downward solar radiation. The possible deviations in surface energy and SWE over the TP, caused by plane-parallel assumption in most climate models may result in biases in the liquid runoff and the river water resources over the TP and downstream.

## 1 Introduction

The Tibetan Plateau (TP), or “the third pole on Earth”, has an area of 2.5 million km<sup>2</sup> and an average elevation exceeding 4.5 km, and it plays a crucial role in the Earth’s climate system. As a terrain barrier, the TP not only forces air masses to rise and undergo cooling effect (Liu et al. 2007; Terzago et al. 2014; Wu et al. 2015), but also impacts the thermo-dynamical properties of the atmospheric circulation, energy budget, and global climate (Ding et al. 1992; Wu

et al. 2006, 2015). From the hydrological point of view, the water melted from the snowpack on the TP provides water through the major river systems for 1.5 billion people living downstream (Yao et al. 2012; Terzago et al. 2014). Furthermore, the land surface processes over the TP significantly affect the duration and strength of Asian monsoon systems (Yao et al. 2012).

Spatiotemporal variations in the surface solar radiation over irregular rugged surfaces result from the complex interactions between direct and diffuse solar beams in the atmosphere-surface system, which determine many landscape processes such as soil moistening, evapotranspiration, photosynthesis, and snow melting (Liou et al. 2007, 2013; Lee et al. 2011, 2013; Zhao et al. 2016). Accurate calculating the radiative transfer over complex topography is challenging because of the complexity of the spatial orientation and inhomogeneous features of mountain surfaces. Most current climate models have been using the plane-parallel (PP) assumption to calculate the radiative transfer process in the earth-atmosphere system, i.e., the surface is assumed to be homogeneous and flat in these models. However, Lee et al. (2013) showed that there were significant deviations in

✉ Xuehua Fan  
fxh@mail.iap.ac.cn

<sup>1</sup> Key Laboratory of Middle Atmosphere and Global Environment Observation, Institute of Atmospheric Physics, Chinese Academy of Sciences, Beijing, China

<sup>2</sup> Joint Institute for Regional Earth System Science and Engineering and Department of Atmospheric and Oceanic Sciences, University of California, Los Angeles, CA, USA

<sup>3</sup> Research Center for Environmental Changes, Academia Sinica, Taipei, Taiwan

the surface insolation over the TP between the 3-D radiative transfer scheme, which considers the impact of complex terrain, and the plane-parallel model. The deviations in downward surface solar fluxes between the 3-D model and the PP radiative transfer scheme were approximately  $200 \text{ W m}^{-2}$  at shaded or sunward sides for a clear sky without aerosols. There is also about  $+100 \text{ W m}^{-2}$  deviation in the reflected fluxes of the direct solar radiation over snow covered areas (Lee et al. 2013), which will lead to more snowmelt over the TP.

A parameterization of solar fluxes over complex terrain was developed based on 3-D Monte Carlo photon tracing simulations (Liou et al. 2007; Lee et al. 2011, 2013). This parameterization has been incorporated into the fourth version of the global Community Climate System Model (CCSM4 hereafter) to estimate the impact of complex topography on the surface hydrology over the Sierra Nevada and Rocky Mountains in the western United States (Lee et al. 2015). The 6-year simulation results showed substantial increases/decreases in the downward surface solar flux over mountain tops/valleys. More importantly, the 3-D topography of the Rock Mountain and Sierra Nevada regions is likely to induce faster snowmelt in the mountain tops, thereby leading to a shortened duration of snow cover and different snowmelt-driven runoff amounts at lower elevations.

The TP is characterized by complex terrain. To assess the long-term influence of complex terrain on land surface processes and hydrology over the TP, the CCSM4 with the incorporation of 3-D radiative transfer parameterization is used to analyze the surface solar radiation, cloud cover, snow water equivalent, and runoff in the region. This paper is organized as follows. The 3-D radiation parameterization in the CCSM4 is described in Sect. 2. Section 3 presents the model simulation results, including the spatial patterns in the surface energy, total cloud fraction, precipitation rate, and snow water equivalent (SWE) in January (winter) and April (snow melt season). We also analyze seasonal variations in the total cloud fraction, surface energy and hydrology as a function of elevation in Sect. 3. Finally, a summary is given in Sect. 4.

## 2 Parameterization scheme of 3-D radiative transfer applied in CCSM4

The 3-D parameterization approach was presented in detail in Lee et al. (2011, 2013). Below is a brief review. The solar fluxes reaching the surface physically include following components. The direct and diffuse flux ( $F_{\text{dir}}$ ,  $F_{\text{dif}}$ ) represent photons striking the ground directly from the sun without experiencing scattering or reflection and photons undergoing single and/or multiple atmospheric scattering,

respectively. The direct and diffuse reflected flux ( $F_{\text{rdir}}$ ,  $F_{\text{rdif}}$ ) represents the reflection of  $F_{\text{dir}}$  and  $F_{\text{dif}}$  from neighboring surfaces, respectively. Radiation experiencing surface reflection or atmospheric scattering after having been reflected by the ground is the coupled flux ( $F_{\text{coup}}$ ). The objective of the 3-D parameterization is to produce the relative deviations in the five components from those calculated by a conventional PP radiative transfer model, given subgrid-scale topographic information. The corresponding relative deviations in the direct, diffuse, and coupled fluxes are defined as follows:

$$F'_i = \frac{F_i - \hat{F}_i}{\hat{F}_i}, \quad i = \text{dir, dif, coup}, \quad (1)$$

where  $F_i$  is the surface flux calculated from the 3-D Monte Carlo model, and  $\hat{F}_i$  is the flux from the PP radiative transfer scheme. Since  $\hat{F}_{\text{rdir}}$  and  $\hat{F}_{\text{rdif}}$  are zero, the relative deviations in the  $F_{\text{rdir}}$ ,  $F_{\text{rdif}}$  are set as follows:

$$F'_{\text{rdir}} = \frac{F_{\text{rdir}}}{\hat{F}_{\text{dir}}}, \quad \text{and} \quad F'_{\text{rdif}} = \frac{F_{\text{rdif}}}{\hat{F}_{\text{dif}}}. \quad (2)$$

Several topographic parameters including the cosine of the solar incident angle ( $\mu_i$ ), the sky view factor (the portion of the sky dome visible to the target point,  $V_d$ ), and the terrain configuration factor (the area of surrounding mountains visible to the target point,  $C_t$ ) were introduced as the independent variables for multiple linear regression analysis (Lee et al. 2013). Using multiple linear regression analysis, the relative deviations in the five components of the surface fluxes are expressed by a linear combination of the topographic parameters. To improve the regression parameterization, the normalized variables are defined as follows:

$$\tilde{\mu}_i = \frac{\mu_i}{\cos \theta_s}, \quad \tilde{V}_d = \frac{V_d}{\cos \theta_s}, \quad \text{and} \quad \tilde{C}_t = \frac{C_t}{\cos \theta_s}, \quad (3)$$

where  $\theta_s$  is the slope angle of the surface. Following Lee et al. (2013), the relative deviations ( $F'_i$ ,  $i = \text{dir, dif, rdir, rdif, coup}$ ) in the five components for a clear sky can be expressed as follows:

$$\begin{pmatrix} F'_{\text{dir}} \\ F'_{\text{dif}} \\ F'_{\text{rdir}} \\ F'_{\text{rdif}} \\ F'_{\text{coup}} \end{pmatrix} = \begin{pmatrix} a_1 \\ a_2 \\ a_3 \\ a_4 \\ a_5 \end{pmatrix} + \begin{pmatrix} b_{11} & b_{12} & 0 & 0 \\ b_{21} & b_{22} & 0 & b_{24} \\ 0 & b_{32} & b_{33} & 0 \\ 0 & b_{42} & b_{43} & 0 \\ b_{51} & b_{52} & b_{53} & 0 \end{pmatrix} \begin{pmatrix} \langle \tilde{\mu}_i \rangle \\ \langle \tilde{V}_d \rangle \\ \langle \tilde{C}_t \rangle \\ \sigma(h) \end{pmatrix}, \quad (4)$$

where  $a_i$  is the interception,  $b_{ij}$  is the regression coefficient for a specific independent variable, and  $\sigma(h)$  is the standard

deviation of the elevation  $h$ . The derived deviations can be applied in any climate models to interpret the impact of complex terrain on the distribution of solar radiation. To improve the accuracy of the parameterization, the topography data at a resolution of  $\sim 90$  m from the Shuttle Radar Topography Mission (SRTM) global data set (Jarvis et al. 2008) was used to carry out 3-D Monte Carlo photon tracing simulations (Lee et al. 2013).

The deviations in the five components between the “exact” values from 3-D Monte Carlo simulations and the values predicted by regression equations were compared to interpreting the precision of the 3-D parameterization (Lee et al. 2011, 2013). The mean solar incident angle and the mean sky view factor in the regression equation explain more than 80% of the variation in the deviation of the direct flux; the root mean square errors (RMSE) are generally less than  $3 \text{ W m}^{-2}$ . The variation in the deviation of the diffuse flux is about  $5 \text{ W m}^{-2}$ , and the RMSE is less than  $0.5 \text{ W m}^{-2}$ . The variation and the RMSE for the deviation in the direct-reflected flux are  $1\text{--}8 \text{ W m}^{-2}$  and  $0.08\text{--}0.5 \text{ W m}^{-2}$ , respectively, depending on the position of the sun. The variation and RMSE for the deviation in the diffuse-reflected flux are approximately 0.3 and  $0.01 \text{ W m}^{-2}$ , respectively. The performance of the regression equations for the coupled flux is less satisfactory because the coupled flux contains photons experiencing multiple scattering more complicated; however, the magnitude of the error is so small that it does not affect the total flux calculation (Lee et al. 2011). Lee et al. (2013) proved that the 3-D radiative transfer scheme can be applied to grid cells coarser than  $10 \times 10 \text{ km}$ .

The CCSM4 is used to investigate the long-term effect of the complex topography on the surface energy, snow cover and hydrology over the TP. The CCSM developed by the National Center for Atmospheric Research (NCAR) is a coupled climate model comprised of separate atmosphere (Community Atmosphere Model, CAM4), ocean (Parallel Ocean Program, POP2), land (Community Land Model, CLM4), and sea ice (Community Ice Code, CICE4) components, plus one central coupler component. The model system was described in detail by Gent et al. (2011). The preceding radiative transfer parameterization has been incorporated into the CCSM4 (Lee et al. 2015).

Focusing on the TP ( $25\text{--}40^\circ\text{N}$ ,  $70\text{--}100^\circ\text{E}$ ) and elevations greater than 1.5 km, two numerical experiments are performed as follows. A simulation with a conventional plane-parallel radiative transfer parameterization is performed as the control experiment. Another experiment was conducted with a 3-D radiative transfer scheme implemented. We have carried out 11-year simulations (from 2000 to 2010) at a horizontal resolution of  $0.23^\circ \times 0.31^\circ$ , with prescribed sea surface temperatures and sea ice, greenhouse gases, and aerosols corresponding to the year 2000. We used the results determined from the last 10 years in the analysis.

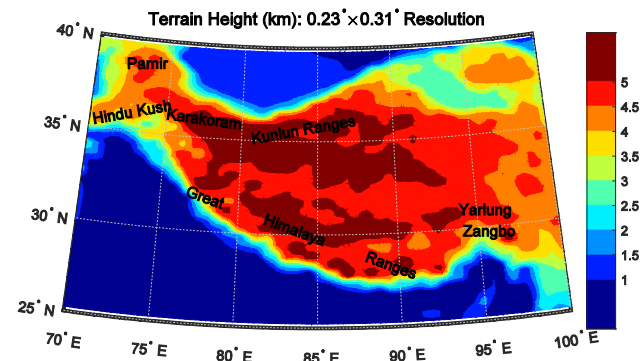


**Fig. 1** The elevation map at a  $0.23^\circ \times 0.31^\circ$  resolution for the Tibetan Plateau

The elevation map of the Tibetan Plateau is displayed in Fig. 1 at a  $0.23^\circ \times 0.31^\circ$  resolution.

### 3 Model simulation results

#### 3.1 Impact of complex topography on the spatial pattern of surface energy and hydrology

Simulation results in March when snows begin to melt over the TP are selected to evaluate the model results with the measurements. Figure 2a displays the March mean SWE map over the TP processed by the Canadian Meteorological Centre (CMC) (Brown and Brasnett 2010). The CMC product is often considered the best available snow products for evaluating modeled output (e.g., Su et al. 2010; Reichle et al. 2011; Toure et al. 2016), which is the reason that we first decided to use CMC product. The CMC snow analysis consists of the NH snow depth data. The snow depth is generated based on a 6-hourly optimal interpolation of an extensive in situ snow depth report from the World Meteorological Organization (WMO) information system (Brasnett 1999). The first-guess field is obtained through a simple snow model driven with 6-hourly meteorological forcing from the European Center for Medium-Range Weather Forecasts (ECMWF) ERA-15 Reanalysis (Brown et al. 2003). The CMC snow depth data were converted to SWE estimates using snow densities (Sturm et al. 2010). In areas with a high density of snow depth observations, the resulting SWE estimates are largely controlled by the observed spatial and temporal variability in snow depth. In data sparse areas, the SWE estimates are entirely simulated from the snowpack model driven with the ECMWF temperature and precipitation fields (Brown et al. 2003). The CMC SWE data have a spatial resolution of 24 km, which is comparable to that of the model. In this study, we used the CMC monthly SWE data for March from 2001 to 2010.

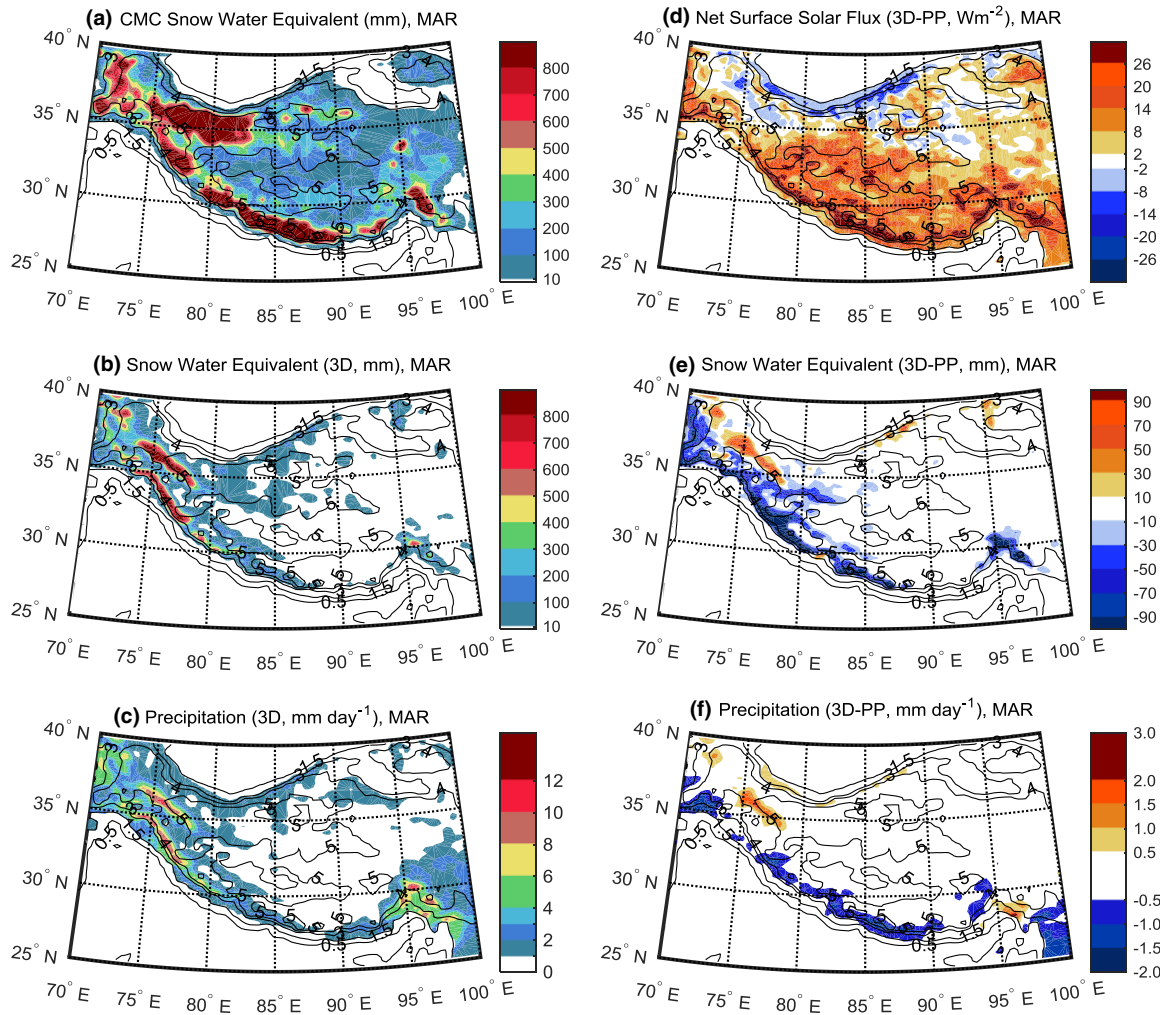


**Fig. 2** The March mean **a** snow water equivalent (SWE) estimated from the Northern Hemisphere daily snow depth data processed by the Canadian Meteorological Centre (CMC), **b** SWE map simulated by 3-D experiment, **c** precipitation map simulated by 3-D experiment,

**d** deviation (3-D-PP) in the net surface solar flux, **e** SWE deviation (3-D-PP) map, and **f** precipitation deviation (3-D-PP) map. The black contour lines are terrain heights in kilometer

The 10-year mean SWE, precipitation rate simulated with the 3-D parameterization and corresponding difference (3-D-PP) over the TP for March are shown in Fig. 2b, c, e, and f respectively. Figure 2d shows the March mean deviation (3-D-PP) of the net surface solar flux (FSNS). The black contour lines in Fig. 2 are terrain heights in km.

Model simulated peaks in the SWE are located in the Hindu Kush, Pamir, Karakoram, Kunlun ranges and the western Himalayas. The SWE values decrease along the Himalayas to the southeast. The spatial pattern in the SWE is consistent with the simulation from the MIROC4h climate model (Terzago et al. 2014). The MIROC4h (the model for interdisciplinary research on climate version 4 with high resolution) developed by University of Tokyo, National Institute for Environmental Studies, and Japan Agency for Marine-Earth Science and Technology is coupled with the

land surface model of the minimal advanced treatments of surface interaction and runoff (MATSIRO) (Takata et al. 2003). It has a spatial resolution of  $0.5625^\circ$  with 56 vertical layers (Sakamoto et al. 2012). Further detailed descriptions of the model configurations are summarized in Sakamoto et al. (2012).

The CMC SWE shows corresponding peak areas similar to those from the CCSM4 simulation, although the CMC exhibits higher SWE values throughout Tibetan Plateau. Toure et al. (2016) evaluated the SWE simulation from CLM4 for the period from Jan. 2001 to Jan. 2011 using CMC snow products. In this study, we also use the standard statistical techniques including mean bias (MB), root-mean square error (RMSE), and anomaly correlation coefficient R to assess the CCSM4 SWE against CMC SWE data. The values of MB, RMSE, and R are  $-139$  mm,  $288$  mm, and

0.10 respectively, which are comparable to the results (MB, RMSE, and R are  $-130$  mm, 134 mm, and 0.08, respectively) by Toure et al. (2016).

However, previous studies reported that very poor coverage of in situ snow depth measurements in the Tibetan Plateau (TP) was available for CMC snow analysis (Fig. 9 in Reichle et al. 2011), which means that CMC estimates for the TP are based mostly on “a simple snow model”. An additional uncertainty was also introduced using snow density parameterization (Sturm et al. 2010) to convert CMC snow depth to SWE (Toure et al. 2016). Therefore, the CMC products over the TP should be interpreted with caution because of the scarcity of the available meteorological observations.

Due to this reason, we further compared the simulated SWE from CCSM4 incorporated with 3-D radiative scheme with the snow depth data from Global Land Data Assimilation System version 2 (GLDAS-2) (Beaudoin and Rodell 2016) and the passive microwave SWE data from Advanced Microwave Scanning Radiometer-Earth Observing System (AMSR-E/Aqua) L3 products (Tedesco et al. 2004). Figure 3a shows the March mean GLDAS snow depth data (2001–2010) of 25 km resolution, and Fig. 3b exhibits the March mean AMSR-E/Aqua L3 SWE data (2003–2010) of 25 km resolution. Compared with these two data sets, CMC significantly overestimates the SWE over the TP, especially over the southern ranges, while the SWE simulated by CCSM4 with 3-D radiative transfer parameterization seems to fall within the ranges of the two sets of observations, with some degrees of overestimate over the southern TP. Previous relevant modeling studies also reported the overestimates of SWE over the TP when comparing their modeling results with other available datasets. Qian et al. (2011) and Toure et al. (2016) showed that the CLM4 model overestimated the snowpack significantly against MODIS observations over the TP. In addition, compared to Interim European Center for Medium-Range Weather Forecasts (ECMWF) Re-Analysis ERA-Interim/Land data, Climate Forecast System Reanalysis (CFSR) data and Twentieth Century Reanalysis version 2 (20CRv2) data, the CCSM4 simulation for mean

winter (DJFMA) during 1980–2005 tends to overestimate the SWE over the highest-elevation mountains of the Hindu Kush-Karakoram and Himalaya (HKKH) regions (Terzaghi et al. 2014). The HKKH regions correspond to the southern ranges over the TP in our study, where the CCSM4 model with the 3-D radiative transfer parameterization shows a reduction in the SWE. Note that every type of SWE data, including the CCSM4 simulations, the CMC products, the GLDAS-2 data, and the AMSR-E/Aqua product may have large uncertainties over the TP. It is currently impossible to identify which data are most accurate over the TP (Toure et al. 2016) due to lack of in situ SWE measurements.

The differences (3-D-PP) in SWE are related to differences in precipitation, FSNS, and surface temperature. The decreased SWE along the Hindu Kush–Karakoram–Himalaya mountain ranges is due to the more available solar flux (Fig. 2d) considering 3-D effects and the reduced precipitation (Fig. 2f). The maximum reductions in SWE (Fig. 2e) reach 90 mm. The negative deviation in precipitation (Fig. 2f) of about 2 mm/day makes the difference of about 60 mm per month. The negative deviation in SWE is partly caused by the reduced precipitation. Zhang et al. (2019) suggested that many climate models (including CCSM4) have exaggerated the scaling value of precipitation in southeastern Qinghai-Tibet Plateau compared with the observed values. Thus, in combination with our results, it can indicate that 3-D scheme has its advantages for the area with complex terrain, such as TP. The positive deviations in the precipitation at the Yarlung Zangbo Valley correspond to the negative deviations in SWE because the FSNS (Fig. 2d) increased due to the 3-D mountain effects. The significant reduction in SWE corresponds to a reduction in the reflected solar radiation (not shown here). The decreased SWE results in a reduced surface albedo, and a lower reflected solar radiation.

The snow season normally begins in mid-September over the TP and snow continues to accumulate after this point, with the maximum accumulation occurring in January (Qin et al. 2006; Qian et al. 2011). April is the middle of the snow ablation season (Yao et al. 2012). Therefore,

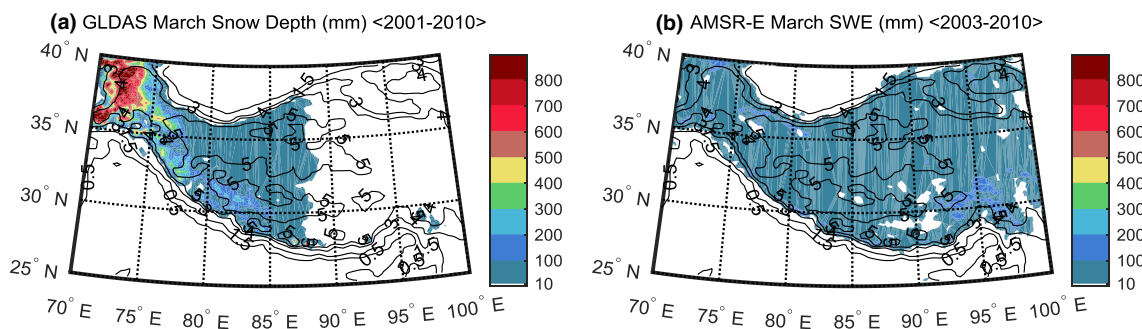


**Fig. 3** The March mean **a** GLDAS snow depth data (2001–2010), and **b** AMSR-E/Aqua L3 SWE data (2003–2010) of 25 km resolution

January and April were selected to examine the 3-D effects on the surface energy and hydrology over the TP. The 10-year mean FSNS value over the TP for winter (January)

and spring (April) simulated with the incorporation of the 3-D parameterization are shown in Fig. 4a, b, respectively. The corresponding deviations (3-D-PP) are exhibited in

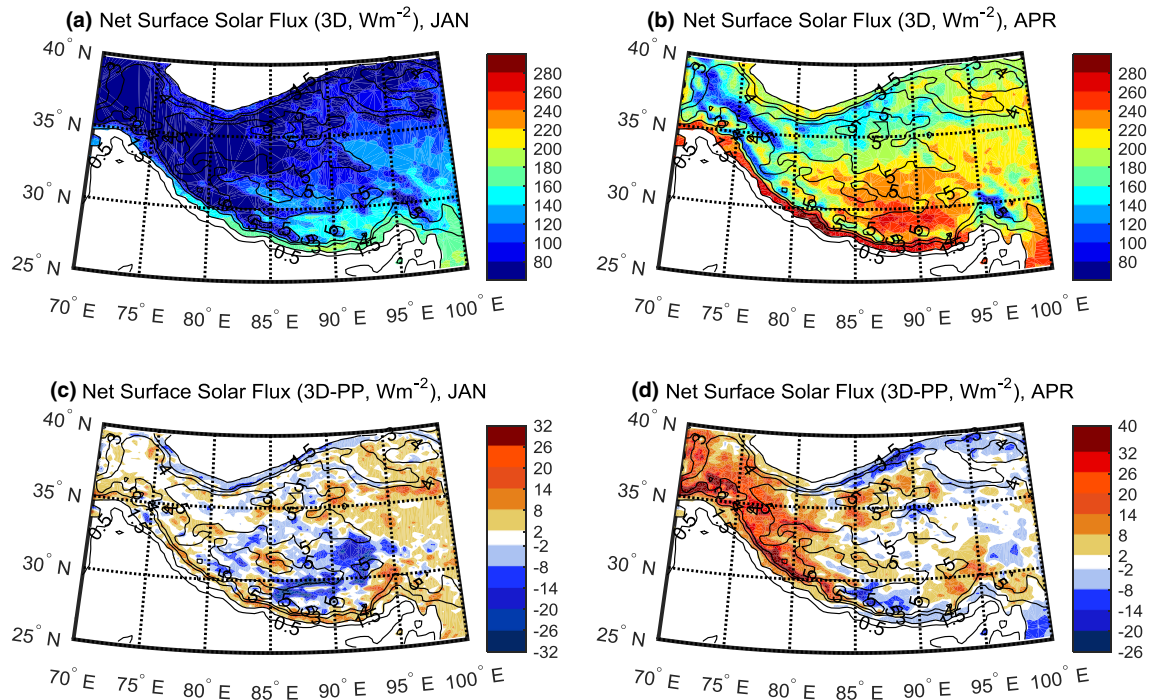


**Fig. 4** The 10-year mean net surface solar flux (FSNS) over the TP for January (a) and April (b) simulated with the incorporation of a 3-D parameterization and the corresponding deviations (3-D-PP) in January (c), and April (d)

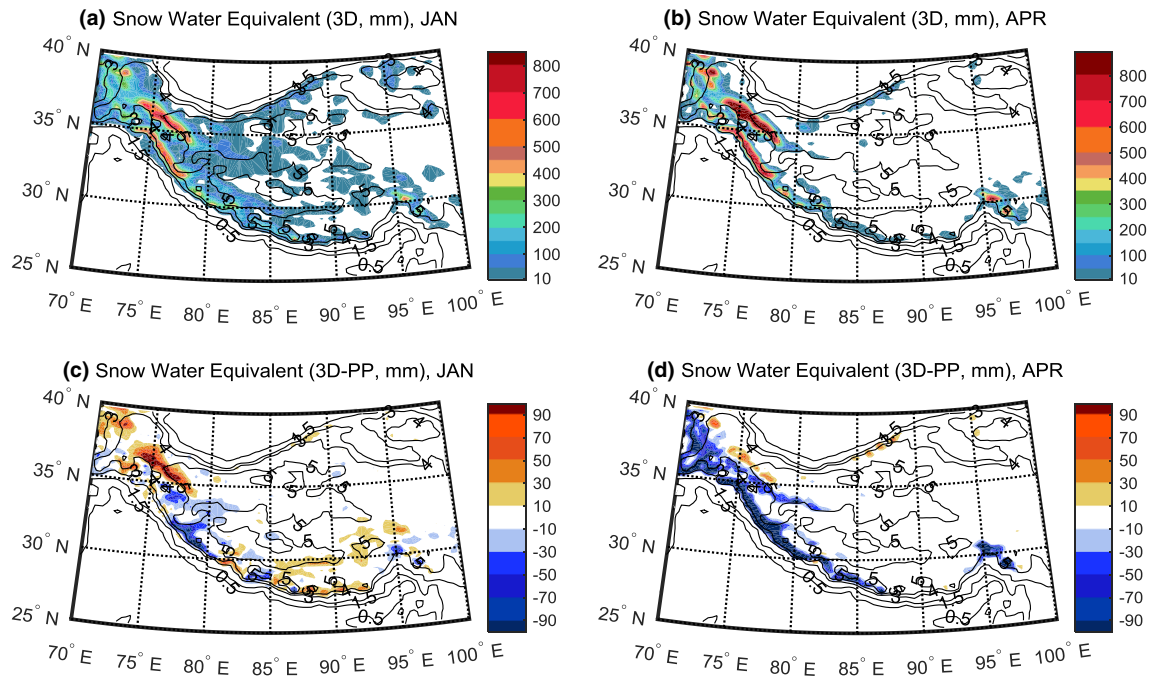


**Fig. 5** Similar to Fig. 4 except for snow water equivalent

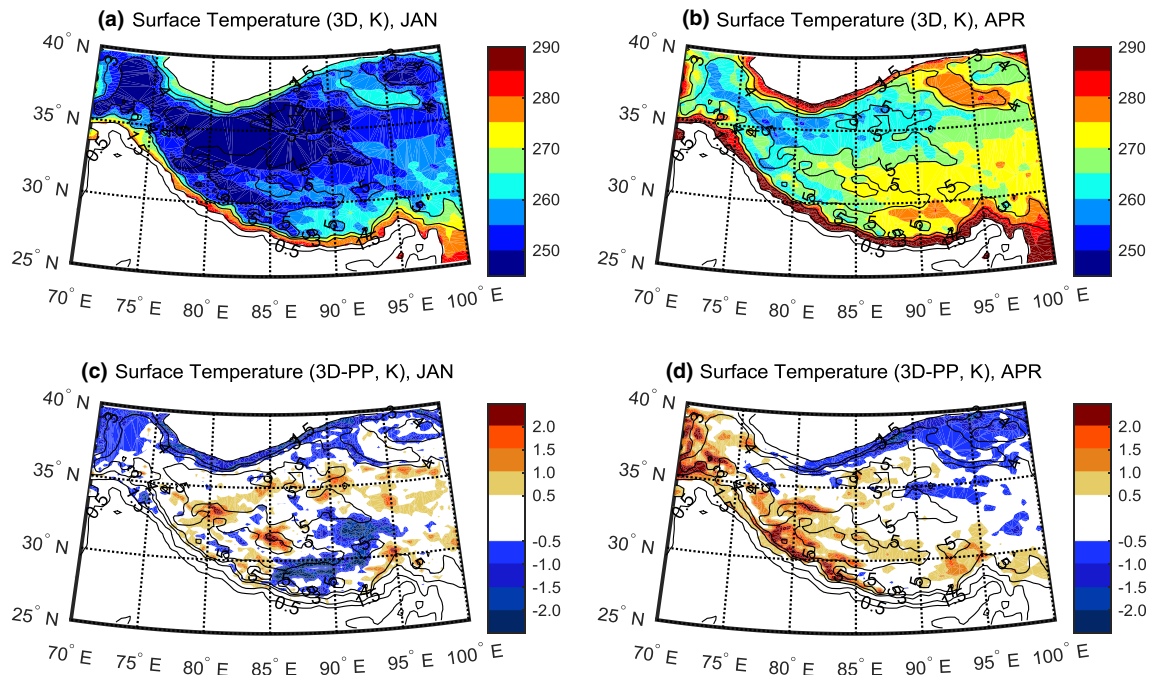


**Fig. 6** Similar to Fig. 4 except for surface temperature

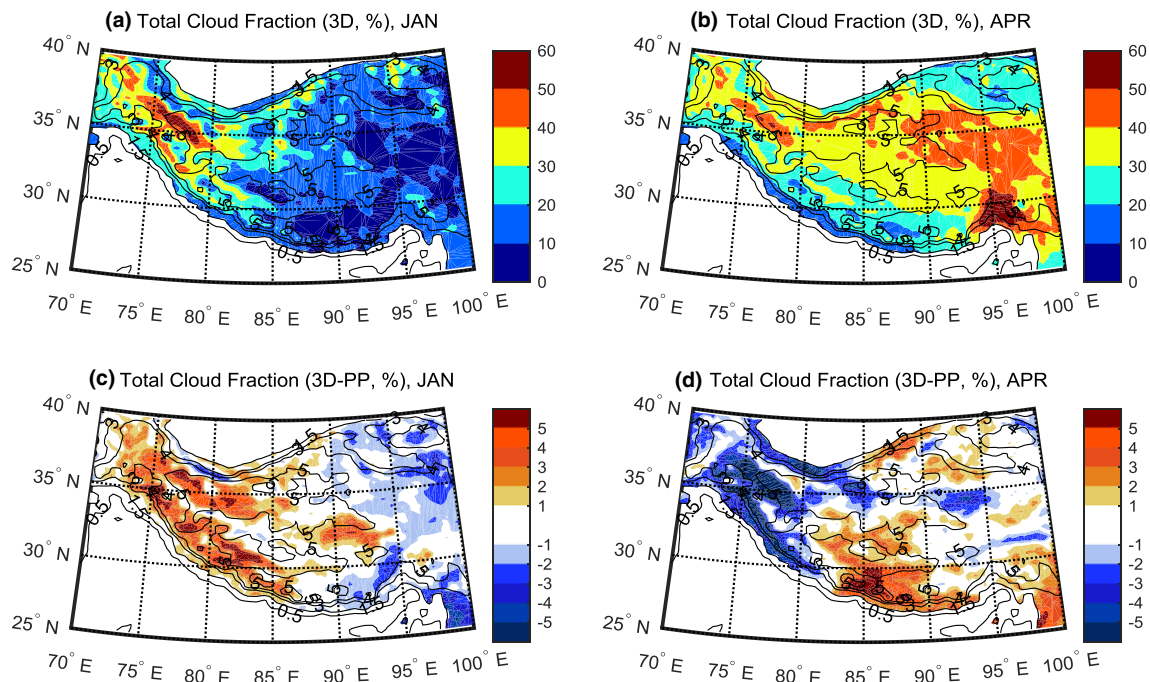


**Fig. 7** Similar to Fig. 4 except for total cloud fraction

Fig. 4c, d. Similarly, Figs. 5, 6 and 7 show the SWE, surface temperature, total cloud fraction over the TP from 3-D experiment and their corresponding deviation (3-D-PP) for January and April. There is an obvious increase in the net surface solar flux over the entire TP from January to

April related to the position of the sun. The FSNS (downward surface solar flux minus upward surface solar flux) is also influenced by the surface albedo, the 3-D topography effect, and cloud fraction. The FSNS exhibited an opposite pattern to that of the SWE (Fig. 5a, b) and cloud fraction

(Fig. 7a, b). Generally, a higher cloud fraction reduces the downward surface solar flux and leads to a lower FSNS. Lower solar energy absorbed by surface can affect the surface temperature and cause a higher SWE and a higher snow albedo. Then, a higher snow albedo causes more flux to be reflected (higher upward surface solar flux), which results in a lower FSNS.

Most of the TP is covered by snow in January (Fig. 5a), when the surface temperature (Fig. 6a) is below 270 K over the entire TP. In April, the SWE peaks are still located at the northwestern part of the TP and the western part of Yarlung Zangbo valley in the east-southern region of the TP, where the surface temperature is below the freezing point, as shown in Fig. 6b. Larger cloud fractions are found in the northwest part of the TP in January (Fig. 7a), which corresponds to the lower net surface solar flux (Fig. 4a). The Karakoram and Pamir regions receive large amount of precipitation during winter (December–January) season (Dimri 2009; Mausson et al. 2014) where clouds generally present in January (Fig. 7a), additional surface heating from the 3-D mountain effect could help to enhance cloud fraction (Fig. 7c).

The differences between the 3-D and PP in the FSNS (Fig. 4c, d) are due to the effects of topography, the differences in the snow field (Fig. 5c, d), and the differences in cloud amounts (Fig. 7c, d). Positive deviations in the FSNS in January generally occur over the south slopes of mountains and mountain summits, where more solar flux is intercepted. During the winter in the Northern hemisphere, the sun rises from the south east and sets in the southwest. And, the solar zenith angle, another astronomical factor influencing FSNS, has the smaller daily minimum value in April than that in January. Thus, more solar radiation is intercepted by the south slopes (sunny side) of the mountains in January than April. Therefore, positive deviations (3-D–PP) in the FSNS in the winter occur over the south slopes of mountains. The downward solar flux deviations appear to be negative over valleys and the north slopes of mountains, especially along the northern margin of the TP, due to the shadow effects during wintertime.

The deviations (3-D–PP) in the total cloud fraction in January shown in Fig. 7c display an increased cloud fraction at higher-elevation ( $> 4.0$  km) areas, where the net surface solar fluxes is reduced (Fig. 4c). The total cloud fraction is largely driven by the changes of low clouds fraction over the TP (Duan and Wu 2006; Pan et al. 2017). These low clouds likely developed in response to the solar heating, which gradually built up since the sunrise (Gu et al. 2012). As is common in mountain environments, upslope flows contribute to convection and cloud formation as the elevated surface in mountains was heating up relative to the surrounding air. During winter, westerly winds bring moisture from the Mediterranean and Caspian Sea to the TP (Syed et al. 2006; Zhang et al. 2013), which is in favor of cloud formation,

and additional surface heating from the 3-D mountain effect could help to enhance cloud fraction.

The positive deviations (3-D–PP) in the FSNS in April (in Fig. 4d) along the Hindu Kush–Karakoram–Himalaya mountain ranges correspond to negative deviations (3-D–PP) in the SWE (Fig. 5d), which indicates that the enhanced net surface solar flux results in decreased SWE and the reduced SWE lowers the surface albedo and increases the net solar flux reaching at surface. Negative deviations (3-D–PP) in the SWE, generally greater than 70 mm, are found along the Hindu-Kush, Karakoram, Kunlun mountain ranges, and the western Himalayas in April (Fig. 5d). Clouds increase over the southern TP but decrease over the western part in April (Fig. 7d).

The deviations (3-D–PP) in the clear-sky surface solar flux (FSNSC) and reflected solar radiation for January and April are shown in Fig. 8a, b, e, f. The deviations in the FSNSC show a similar pattern of deviations in the FSNS (Fig. 4c, d). The FSNSC is relative to the orography effects and the change in the snow field. In January, positive/negative deviations (3-D–PP) in the FSNSC are found at south/north slopes over the TP because the 3-D mountain effects are dominated. The deviations in the FSNSC in January are similar to those in April over the Hindu-Kush, Karakoram mountain ranges, and the western Himalayas, as well as the western part of Yarlung Zangbo valley. For these regions, the FSNSC shows positive deviations in January and April; the deviations in April have larger magnitudes. The remarkable decreases in SWE in April for these regions correspond to reductions in the reflected solar radiation (Fig. 8f). The decreased SWE results in a reduced surface albedo; the lower snow albedo causes less solar radiation to be reflected.

Differences between the 3-D–PP deviations of the FSNSC and FSNS are shown in Fig. 8c for January, and in Fig. 8d for April, to illustrate the possible effects of changes in cloud fields induced by the 3-D effect. Changes in clouds contribute to the differences between the FSNS and FSNSC. Thus, the 3-D–PP deviations in cloud fraction (Fig. 7c, d) show a pattern opposite to the differences in the deviations between the FSNS and FSNSC, as shown in Fig. 8c, d.

The cloud fraction increases due to 3-D effects over the western TP in January (Fig. 7c), and the 3-D–PP deviations in FSNS also show positive values in the same region. However, the relationship between the 3-D–PP deviations in FSNS (Fig. 4d) and cloud fraction (Fig. 7d) in April is opposite to that in January over the western TP. It is because that the effect of 3-D topography on FSNS plays a more important role than cloud cover changes in January. But the effects of cloud cover changes on the FSNS are dominant in April.

The differences in the 3-D effects between January and April are mainly related to the position of the sun, which results in differences in the surface downward solar flux, surface temperature, surface albedo, cloud changes and so

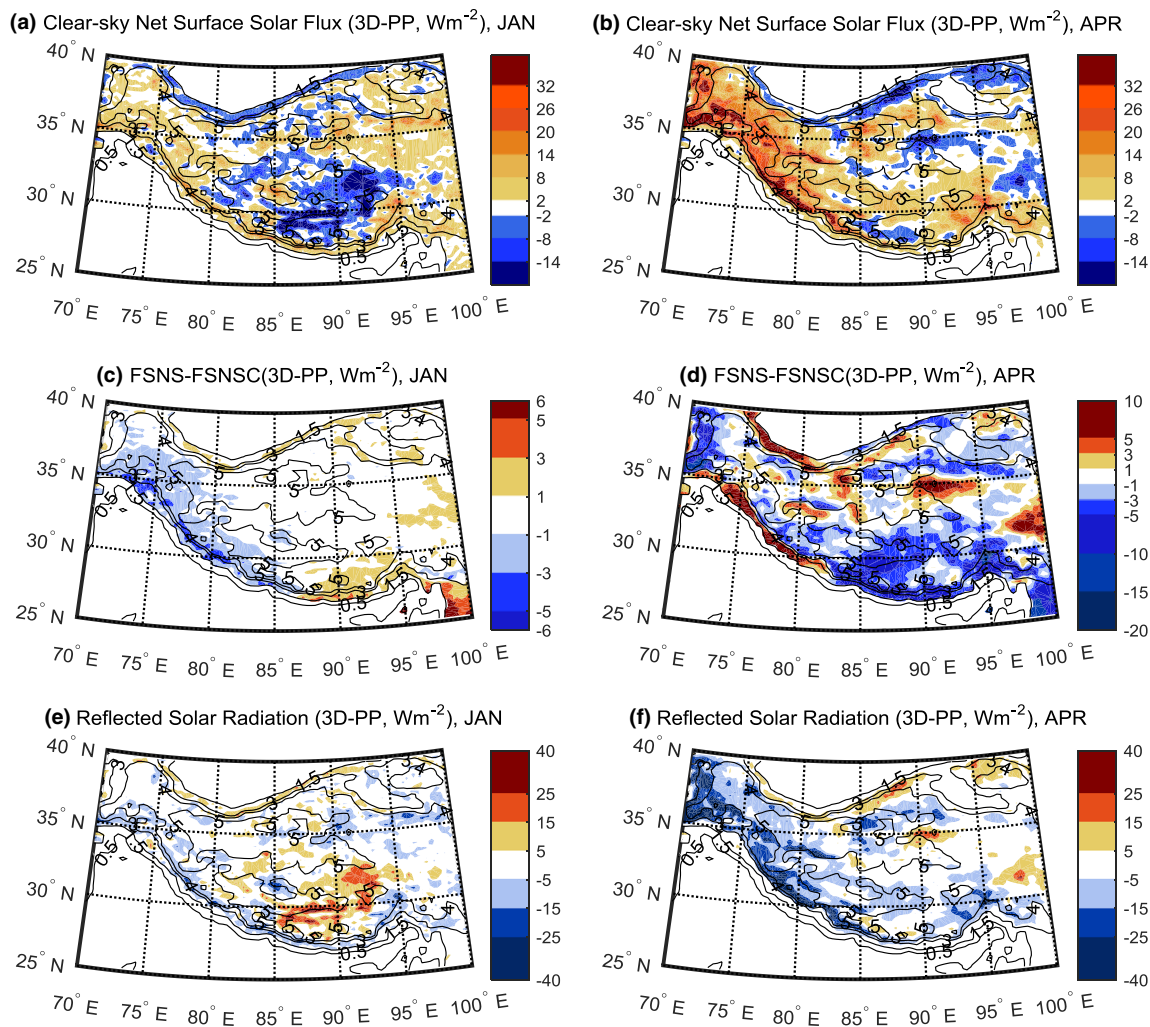


**Fig. 8** The deviations (3-D-PP) in the 10-year mean clear-sky net surface solar flux (FSNSC) for January (a) and April (b). The map of differences between the FSNS deviations and the FSNSC deviations

in January (c) and April (d). The deviations (3-D-PP) in the 10-year mean reflected solar radiation (FSR) over the TP for January (e) and April (f)

on. In April, the differences in the solar radiation due to topography become weaker compared with those in January because the sun moves north. And, the differences between the 3-D-PP deviations of the FSNSC and FSNS are within the ranges of  $-6$  to  $+6 \text{ W m}^{-2}$ ,  $-20$  to  $+10 \text{ W m}^{-2}$  in January (Fig. 8c), and April (Fig. 8d), respectively. The 3-D-PP deviations of the FSNS take values from  $-32$  to  $+32 \text{ W m}^{-2}$  (Fig. 4c),  $-26$  to  $+40 \text{ W m}^{-2}$  (Fig. 4d) in January, and April, respectively. It means that differences in the 3-D-PP deviations of the FSNSC and FSNS for April (Fig. 8d) are more pronounced compared to those in January (Fig. 8c), suggesting cloud cover change is a dominant effect in April.

Atmospheric circulation plays an important role on cloud formation; therefore, the vertical velocity and horizontal wind vectors are used to investigate the 3-D effects on cloud fraction. Figure 9 shows January (Fig. 9a) and April (Fig. 9b) temperature contours overlain by vertical (unit:

$0.01 \text{ Pa/s}$ ) and meridional (unit:  $\text{m/s}$ ) wind vectors from a 3-D experiment on an  $85^\circ\text{E}$  longitude cross section. The corresponding 3-D-PP deviations for January and April are shown in Fig. 9c, d, respectively. The downward motions are dominant south of  $34^\circ\text{N}$  latitude in January (Fig. 9a), which corresponds to the less cloud fraction shown in Fig. 7a. The vertical motions are upward over  $34^\circ$ – $40^\circ\text{N}$  in Fig. 9a, which results in more cloud fraction shown in Fig. 7a. Compared to vertical motions in January, the ascending motions occur at more southerly location ( $\sim 29^\circ\text{N}$ ) in April, as shown in Fig. 9b, although descending motion still exists at  $32$ – $34^\circ\text{N}$ . This motion results in greater transfer of heat upward and favors the formation of clouds at  $\sim 29^\circ\text{N}$ , as shown in Fig. 7b.

A positive temperature deviation is found at approximately  $300$ – $500 \text{ hPa}$  over  $26$ – $32^\circ\text{N}$  in January (Fig. 9c). The increased heat leads to increased upward motion, corresponding to enhanced cloud fraction in the region, as shown

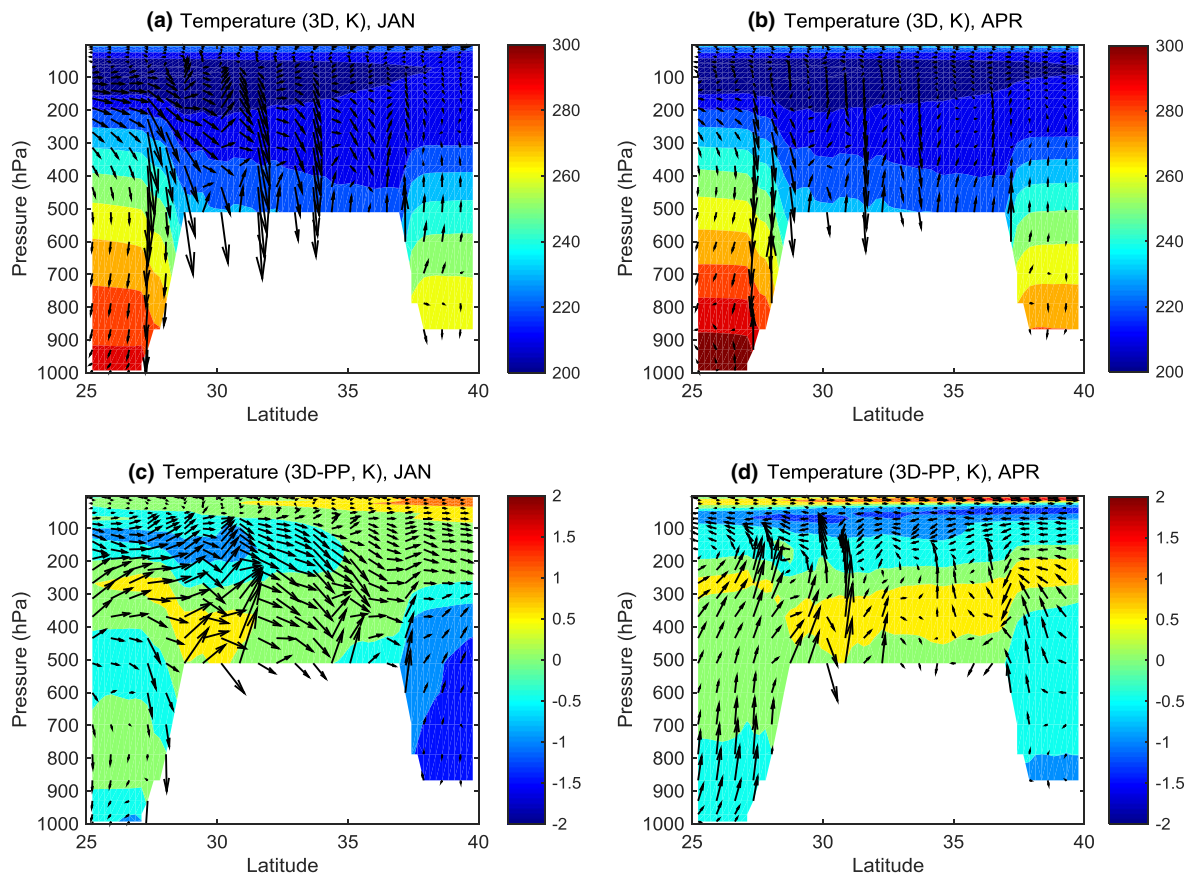


**Fig. 9** Temperature contours overlain by vertical (in  $0.01 \text{ Pa s}^{-1}$ ) and meridional (in  $\text{m s}^{-1}$ ) wind vectors from a 3-D experiment from an  $85^\circ\text{E}$  longitude cross section for January (a) and April (b). The corresponding 3-D-PP deviations in January (c) and April (d)

in Fig. 7c. The 3-D-PP deviations in circulation show dominant upward motions over  $34\text{--}40^\circ\text{N}$ , which also corresponds to positive deviations in the cloud fraction in these regions (Fig. 7c). Similarly, the upward/downward motion in April (Fig. 9d) corresponds to positive/negative deviations in cloud fraction, as shown in Fig. 7d. Increases in clouds over the south region ( $27\text{--}33^\circ\text{N}$ ) of the TP in April, correspond to the upward motions (Fig. 9d).

### 3.2 The elevation-dependent seasonal variation of surface energy and hydrology

Figure 10 exhibits the deviations (3-D-PP) in the monthly averaged net surface solar flux (Fig. 10a), sensible heat flux at surface (Fig. 10b), total cloud fraction (Fig. 10c), and surface temperature (Fig. 10d) as a function of elevation. Variations in the FSNS affect the cloud formation, which leads to changes in the surface energy balance. Thus, the seasonal pattern of deviations in the FSNS is opposite to that of the deviations in the total cloud fractions. Increased/decreased FSNS (Fig. 10a) corresponds to a decreased/increased cloud fraction (Fig. 10c). Differences in the FSNS are mostly

positive except in December when the total cloud fraction increases significantly. The differences generally increase with elevation, reaching a maximum at higher elevations for the months of February and March, which indicates that more solar flux is intercepted at higher elevation regions due to 3-D topography effects. Total cloud fractions for most of the year decrease due to 3-D mountain effects, except in May and December. Mountain clouds normally develop in response to surface solar heating. The reduced solar insolation in lower elevations due to the 3-D mountain effect tends to cool the surface and weaken the convection over mountain regions, resulting in less cloud water. Since cloud formation is primarily dominated by dynamical processes, enhanced surface heating over mountain tops due to the 3-D effect may not be sufficiently large to initiate cloud formation (Gu et al. 2012). During May when the surface is heated up, or during winter (December–January) which is the snowy season over the Karakoram and Pamir regions (Dimri 2009; Maussion et al. 2014) where clouds generally present in January (Fig. 7a), additional surface heating from the 3-D mountain effect could help to enhance cloud fraction (Fig. 7c). The deviations (3D-PP) in the surface sensible heat flux and

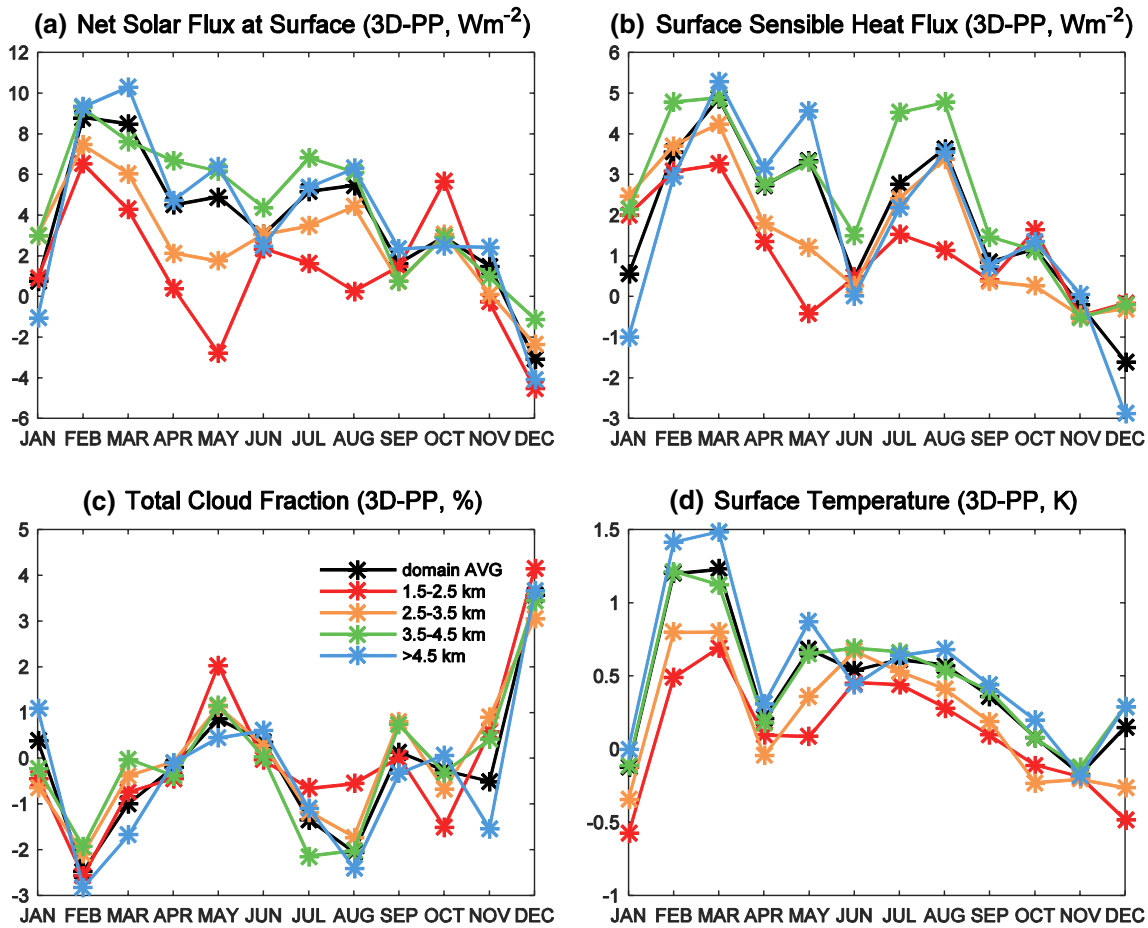


**Fig. 10** Deviations (3-D-PP) in the monthly averaged **a** net surface solar flux, **b** surface sensible heat flux, **c** total cloud fraction, and **d** surface temperature as a function of elevation for 1.5–2.5 km (red),

2.5–3.5 km (orange), 3.5–4.5 km (green), above 4.5 km (blue), and the whole domain excluding pixels lower than 1.5 km (black)

surface temperatures show similar seasonal variations to the deviations (3D-PP) in the net surface solar flux (Fig. 10b, d).

Figure 11 shows the monthly averaged SWE, precipitation rate, runoff, and the corresponding deviations (3-D-PP) over the TP as a function of elevation. The SWE begins to decrease in March, with the peak in February; the exception is 3.5–4.5 km, which the peak is in March and the decrease begins in April. The largest SWE is located over the 3.5–4.5 km elevation region instead of the highest elevation (> 4.5 km) from December to the following April because of several factors. The precipitation (Fig. 11b) for 3.5–4.5 km during the period of December–April is more than that for the elevation > 4.5 km, where moisture is significantly depleted due to rainout at lower elevation. The net solar flux intercepted at mountain tops is much greater than that at lower elevations due to the effects of topography, resulting in more snowmelt at mountain tops. Additionally, blowing snow events in the winter caused by strong westerly winds at upper levels also contribute to the decrease in the snowpack at mountain summits (Moore 2004). Simulations

by the WRF model with a 3-D parameterization over the Rocky Mountains and Sierra Nevada in the western US also have shown peaks in precipitation and SWE values at 2.5–3.0 km instead of at the highest elevations > 3.0 km (Liou et al. 2013).

The decreases in SWE due to topography effect are found during spring months (Fig. 11d) due to the increased downward solar flux (Fig. 10a) and the enhanced surface temperature (Fig. 10d). The changes in the surface solar radiation due to the complex terrain result in earlier snowmelt over the TP. The deviations in the SWE clearly depend on terrain elevations. The SWE is reduced by 1–17 mm due to the 3-D mountain effects in April, with the largest decrease in the SWE in the 3.5–4.5 km elevation. Kim et al. (2007) indicated that the net surface solar flux can have remarkable effects on snowmelt when the low-level temperatures are near their freezing point, at which point a small change in the net surface solar flux could possibly bring the surface temperature above or below the freezing point and influence the snowmelt process. The surface temperature (not

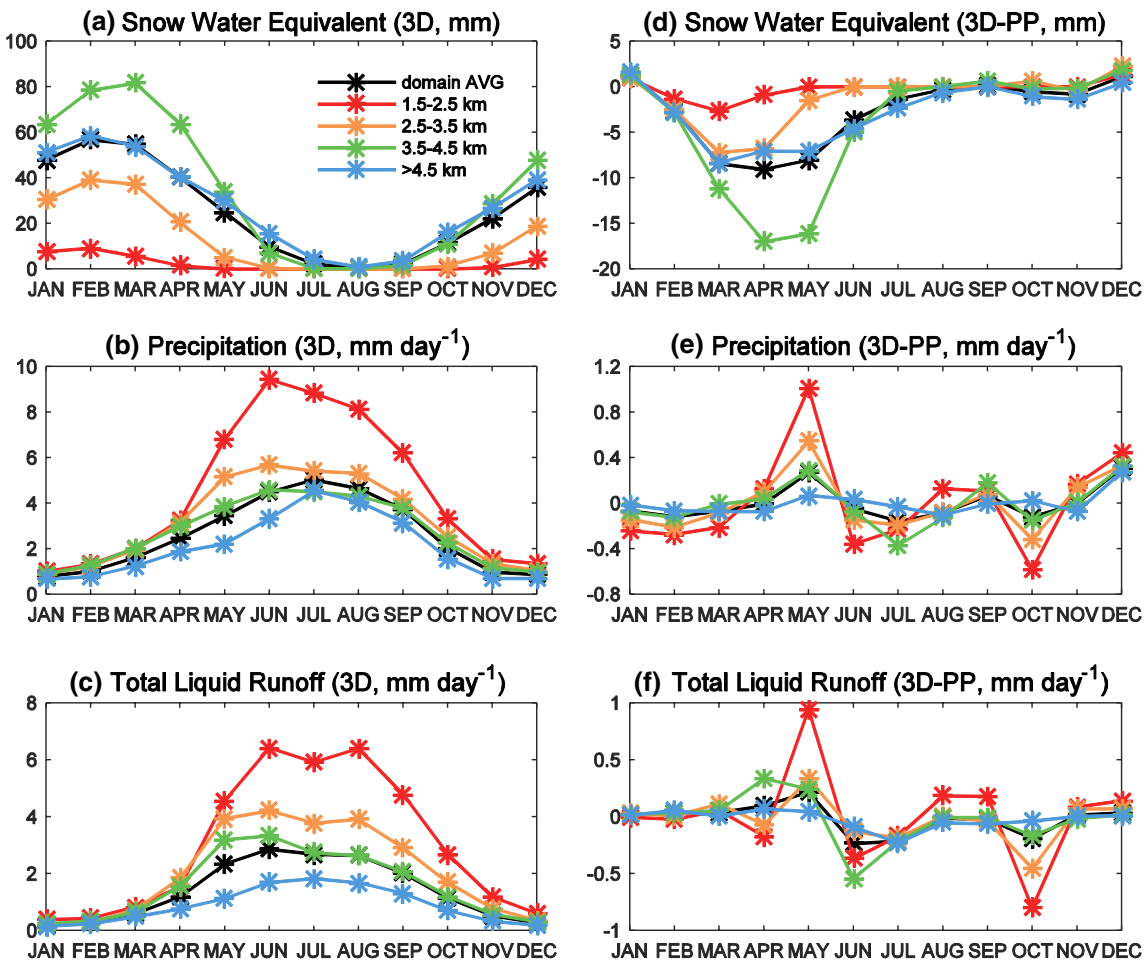


**Fig. 11** The seasonal variation in the **a** snow water equivalent (SWE, mm), **b** precipitation (mm per day), **c** runoff (mm per day) and the corresponding deviations (3-D-PP) in **d** SWE, **e** precipitation, and **f** runoff averaged over the simulation domain excluded those pixels

shown here) in the 3.5–4.5 km elevation range varies near the freezing point over the TP during the period of April and May. This dependence on the ambient temperature explains the elevation dependency of the complex terrain effect on spring SWE over the TP.

Most precipitation occurs during the summer months of rain season, which is influenced by the Asian summer monsoon, and precipitation decreases with elevation. The seasonal variation in the total runoff (Fig. 11c) follows that of precipitation, which suggests that precipitation is a dominant factor for runoff over the TP. Negative deviations in the precipitation rate are found throughout the year, except in May and December (Fig. 11e), and they follow the seasonal variation in the deviations in the total cloud fraction (Fig. 10c). Increased precipitation in May ranges from 0.25 (3.5–4.5 km elevation) to 1.10 mm per day (1.5–2.5 km elevation). The deviations in the total liquid runoff (Fig. 11f) are influenced both by changes in the SWE and by precipitation. The total

lower than 1.5 km as a function of elevation for 1.5–2.5 km (red), 2.5–3.5 km (orange), 3.5–4.5 km (green), above 4.5 km (blue), and the whole domain (black)

liquid runoff for 3.5–4.5 km elevation increases by 0.3 mm per day in April due to earlier (March) snowmelt caused by increased downward solar radiation. The deviations in the total liquid runoff generally follow the seasonal variations in the precipitation over the TP during other months.

## 4 Summary

The CCSM4 model in corporation with a 3-D radiative transfer scheme is used to investigate the long-term impact of complex topography on surface energy and hydrology over the Tibetan Plateau. The 11-year PP and 3-D experiments are performed and the results from the last 10 years are analyzed. The simulation results verified complex terrain imposes a remarkable impact on the surface energy and the water resources of the TP. Positive deviations in the surface downward solar flux in January generally are

found over the south slopes of mountains and mountain tops, where more solar flux is intercepted. However, surface downward solar fluxes over north slopes of mountains or valleys, especially in the northern margin of the TP, presents negative deviations due to the shadow effects during winter. Changes in the surface solar radiation influence the cloud amount and snow cover, which affect the surface energy budget. Thus, the deviations in the total cloud fraction and the SWE exhibit opposite patterns to that of FSNS.

The differences in the 3-D effects between January and April are mainly related to the position of the sun. In April, the difference in solar radiation due to the topographic effect becomes weaker compared with that of January because the sun is more northerly.

The total cloud fraction is mostly reduced throughout the year except in May and December due to the decreased solar flux intercepted at lower elevations, which is caused by 3-D terrain effects. The SWE reaches its maximum value over the TP in February in all elevation ranges except at 3.5–4.5 km, where the maximum value of SWE is in March. The largest values of SWE are located from 3.5–4.5 km instead of the highest elevation >4.5 km because the downward solar flux reaching at mountain tops is much more than that at lower elevation due to 3-D mountain effect, which results in more snowmelt. In addition, the precipitation for 3.5–4.5 km from December to the following April is more than that for elevations >4.5 km. The SWE decreases due to the 3-D mountain effect during the spring months and these decreases clearly depend on terrain elevations. The SWE decreased by 1–17 mm over the TP due to the effects of the complex terrain in April, with the largest decrease in the SWE over the 3.5–4.5 km elevation region. Most precipitation occurs during the summer rain season influenced by the Asian monsoon and precipitation decreases with elevation. Negative deviations in the precipitation rate are found throughout the year, except in May and December, following the seasonal variation in the deviations in the total cloud fraction. The total liquid runoff at 3.5–4.5 km elevation increases in April due to earlier (March) snowmelt caused by increased downward solar radiation.

The 10-year simulation results show that the deviations in the surface energy and in the SWE over the TP are caused by the plane-parallel assumption in most climate models, which may result in uncertainties in the liquid runoff and river water resources on the TP and downstream.

**Acknowledgements** This research was supported by the second Tibetan Plateau Scientific Expedition and Research Program (STEP), Grant No. 2019QZKK0604; National Natural Science Foundation of China Granting Nos. 41475027, 41775033 and China Scholarship Council. Yu Gu is supported by the NSF AGS-1701526, and also acknowledges the support of the Natural Science Foundation of Jiangsu Province, China (No. BK20171230).

## References

Beaudoin H, Rodell M, NASA/GSFC/HSL (2016) GLDAS Noah Land Surface Model L4 monthly  $0.25 \times 0.25$  degree V2.1. Goddard Earth Sciences Data and Information Services Center (GES DISC), Greenbelt

Brasnett B (1999) A global analysis of snow depth for numerical weather prediction. *J Appl Meteorol* 38:726–740

Brown RD, Brasnett B (2010) Canadian Meteorological Centre (CMC) daily snow depth analysis data, Version 1. [2001–2010]. Boulder, Colorado USA. NASA National Snow and Ice Data Center Distributed Active Archive Center. <https://doi.org/10.5067/W9FOYWH0EQZ3>. Accessed 10 Mar 2017

Brown RD, Brasnett B, Robinson D (2003) Gridded North American monthly snow depth and snow water equivalent for GCM evaluation. *Atmos Ocean* 41(1):1–14

Dimri AP (2009) Impact of subgrid scale scheme on topography and landuse for better regional scale simulation of meteorological variables over the western Himalayas. *Clim Dyn* 23:565–574

Ding Y (1992) Effects of the Qinghai-Xizang (Tibetan) Plateau on the circulation features over the plateau and its surrounding areas. *Adv Atmos Sci* 9:113–130

Duan AM, Wu GX (2006) Change of cloud amount and the climate warming on the Tibetan Plateau. *Geophys Res Lett* 33:L22704. <https://doi.org/10.1029/2006GL027946>

Gent PR, Danabasoglu G, Donner LJ, Holland MM, Hunke EC, Jayne SR, Lawrence DM, Neale RB, Rasch PJ, Vertenstein M, Worley PH, Yang ZL, Zhang M (2011) The Community Climate System Model, version 4. *J Clim* 24:4973–4991

Gu Y, Liou KN, Lee WL, Leung LR (2012) Simulating 3-D radiative transfer effects over the Sierra Nevada Mountains using WRF. *Atmos Chem Phys* 12:9965–9976

Jarvis A, Reuter HI, Nelson A, Guevara E (2008) Hole-filled seamless SRTM data (online) V4. International Center for Tropical Agriculture (CIAT)

Kim J, Gu Y, Liou KN (2007) The impact of direct aerosol radiative forcing on surface insolation and spring snowmelt in the southern Sierra Nevada. *J Hydrometeorol* 7:976–983

Lee WL, Liou KN, Hall A (2011) Parameterization of solar fluxes over mountain surfaces for application to climate models. *J Geophys Res* 116:D01101. <https://doi.org/10.1029/2010JD014722>

Lee WL, Liou KN, Wang CC (2013) Impact of 3-D topography on surface radiation budget over the Tibetan Plateau. *Theor Appl Climatol* 113:95–103

Lee WL, Gu Y, Liou KN, Leung LR, Hsu HH (2015) A global model simulation for 3-D radiative transfer impact on surface hydrology over the Sierra Nevada and Rocky Mountains. *Atmos Chem Phys* 15:5405–5413

Liou KN, Lee WL, Hall A (2007) Radiative transfer in mountains: application to the Tibetan plateau. *Geophys Res Lett* 34:L23809. <https://doi.org/10.1029/2007GL031762>

Liou KN, Gu Y, Leung LR, Lee WL, Fovell RG (2013) A WRF simulation of the impact of 3-D radiative transfer on surface hydrology over the Rocky Mountains and Sierra Nevada. *Atmos Chem Phys* 13:11709–11721

Liu YM, Bao Q, Duan AM (2007) Recent progress in the study in China of the impact of Tibetan Plateau on the climate. *Adv Atmos Sci* 24:1060–1076

Maussion F, Scherer D, Molg T, Collier E, Curio J, Finkelnburg R (2014) Precipitation seasonality and variability over the Tibetan Plateau as resolved by the high Asia reanalysis. *J Clim* 19:1820–1833

Moore GWK (2004) Mount Everest snow plume: a case study. *Geophys Res Lett* 31(22):L22102. <https://doi.org/10.1029/2004GL021046>

Pan Z, Mao F, Gong W, Min Q, Wang W (2017) The warming of Tibetan Plateau enhanced by 3D variation of low-level clouds during daytime. *Remote Sens Environ* 198:363–368

Qian Y, Flanner MG, Leung LR, Wang W (2011) Sensitivity studies on the impacts of Tibetan Plateau snowpack pollution on the Asian hydrological cycle and monsoon climate. *Atmos Chem Phys* 11:1929–1948

Qin D, Liu S, Li P (2006) Snow cover distribution, variability, and response to climate change in Western China. *J Clim* 19:1820–1833

Reichle RH, Koster RD, De Lannoy GJM, Forman BA, Liu Q, Mahanama SPP, Toure AM (2011) Assessment and enhancement of MERRA land surface hydrology estimates. *J Clim* 24:6322–6338. <https://doi.org/10.1175/JCLI-D-10-05033.1>

Sakamoto TT, Komuro Y, Ishii M, Tatebe Y, Hasegawa A, Shiogama H, Toyoda T, Mori M, Suzuki T, Mochizuki T, Emori S, Hasumi H, Kimoto M (2012) MIROC4—a new high resolution atmosphere–ocean coupled general circulation model. *J Meteorol Soc Jpn* 90:325–359. <https://doi.org/10.2151/jmsj.2012-301>

Sturm M, Taras B, Liston GE, Derksen C, Jonas T, Lea J (2010) Estimating snow water equivalent using snow depth data and climate classes. *J Hydrometeorol* 11:1380–1394. <https://doi.org/10.1175/2010JHM1202.1>

Su H, Yang ZL, Dickinson RE, Wilson CR, Niu GY (2010) Multi-sensor snow data assimilation at the continental scale: the value of Gravity Recovery and Climate Experiment terrestrial water storage information. *J Geophys Res* 115:D10104. <https://doi.org/10.1029/2009JD013035>

Syed FS, Giorgi F, Pal JS, King MP (2006) Effect of remote forcings on the winter precipitation of central southwest Asia part 1: observations. *Theor Appl Climatol* 86(1–4):147–160. <https://doi.org/10.1007/s00704-005-0217-1>

Takata K, Emori S, Watanabe T (2003) Development of the minimal advanced treatments of surface interaction and runoff. *Glob Planet Change* 38:209–222

Tedesco M, Kelly R, Foster JJ, Chang AT (2004) AMSR-E/Aqua Daily L3 global snow water equivalent EASE-grids, version 2. NASA

National Snow and Ice Data Center Distributed Active Archive Center, Boulder. [https://doi.org/10.5067/AMSR-E/AE\\_DYSNO.002](https://doi.org/10.5067/AMSR-E/AE_DYSNO.002)

Terzago S, Hardenberg JV, Palazzi E, Provenzale A (2014) Snowpack changes in the Hindu Kush–Karakoram–Himalaya from CMIP5 global climate models. *J Hydrometeorol* 15:2293–2313

Toure AM, Rodell M, Yang ZL, Beaudoin H, Kim E, Zhang Y, Kwon Y (2016) Evaluation of the snow simulations from the community land model, version 4 (CLM4). *J Hydrometeorol* 17:153–170

Wu GX, Liu YM, Wang TM, Wan RJ, Liu X, Li WP, Wang ZZ, Zhang Q, Duan AM, Liang XY (2006) The influence of mechanical and thermal forcing by the Tibetan Plateau on Asian climate. *J Hydrometeorol* 8:770–788

Wu GX, Duan AM, Liu YM, Mao JY, Ren RC, Bao Q, He B, Liu B, Hu W (2015) Tibetan Plateau climate dynamics: recent research progress and outlook. *Natl Sci Rev* 2:100–116

Yao T, Thompson LC, Mosbrugger V, Zhang F, Ma Y, Luo T, Xu B, Yang X, Joswiak DR, Wang W, Joswiak ME, Devkota LP, Tayal S, Jilani R, Fayziev R (2012) Third pole environment. *Environ Dev* 3:52–64

Zhang Y, Yu R, Li J, Yuan W, Zhang M (2013) Dynamic and thermodynamic relations of distinctive stratus clouds on the lee side of the Tibetan Plateau in the cold season. *J Clim* 26:8378–8391

Zhang F, Ren H, Miao L, Lei Y, Duan M (2019) Simulation of daily precipitation from CMIP5 in the Qinghai-Tibet Plateau. *SOLA* 15:67–73. <https://doi.org/10.2151/sola.2019-014>

Zhao B, Liou KN, Gu Y, He C, Lee WL, Chang X, Li Q, Wang S, Tseng HR, Leung LR, Hao J (2016) Impact of buildings on surface solar radiation over urban Beijing. *Atmos Chem Phys* 16:5841–5852

**Publisher's Note** Springer Nature remains neutral with regard to jurisdictional claims in published maps and institutional affiliations.